

DOI: 10.1002/ ((please add manuscript number))

Article type: Full Paper

Studies of Functional Defects for Fast Na-ion Conduction in $\text{Na}_{3-y}\text{PS}_{4-x}\text{Cl}_x$ with a Combined Experimental and Computational Approach

*Xuyong Feng, Po-Hsiu Chien, Zhuoying Zhu, Iek-Heng Chu, Pengbo Wang, Marcello Immediato-Scuotto, Hesam Arabzadeh, Shyue Ping Ong, and Yan-Yan Hu**

Dr. X. Feng, P.-H. Chien, P. Wang, M. Immediato-Scuotto, H. Arabzadeh, Prof. Y.-Y. Hu

Department of Chemistry and Biochemistry, Florida State University, 95 Chieftan Way, Tallahassee, FL 32306

Prof. Y.-Y. Hu

Center of Interdisciplinary Magnetic Resonance, National High Magnetic Field Laboratory, 1800 East Paul Dirac Drive, Tallahassee, FL 32310

E-mail: hu@chem.fsu.edu

Z. Zhu, Dr. I.-H. Chu, Prof. S. P. Ong

Department of NanoEngineering, University of California San Diego, 9500 Gilman Drive, La Jolla, CA 92093-0448

This is the author manuscript accepted for publication and has undergone full peer review but has not been through the copyediting, typesetting, pagination and proofreading process, which may lead to differences between this version and the [Version of Record](#). Please cite this article as [doi: 10.1002/adfm.201807951](https://doi.org/10.1002/adfm.201807951).

This article is protected by copyright. All rights reserved.

All-solid-state rechargeable sodium (Na)-ion batteries are promising for inexpensive and high-energy-density large-scale energy storage. In this contribution, new Na solid electrolytes, $\text{Na}_{3-y}\text{PS}_{4-x}\text{Cl}_x$, have been synthesized with a strategic approach, which allows maximum substitution of Cl for S ($x=0.2$) without significant compromise of structural integrity or Na deficiency. A maximum conductivity of 1.96 mS/cm at 25 °C has been achieved for $\text{Na}_{3.0}\text{PS}_{3.8}\text{Cl}_{0.2}$, which is two orders of magnitude higher compared with that of tetragonal Na_3PS_4 (t- Na_3PS_4). The activation energy (E_a) is determined to be 0.19 eV. Ab initio molecular dynamics (AIMD) simulations shed light on the merit of maximizing Cl-doping while maintaining low Na deficiency in enhanced Na-ion conduction. Solid-state nuclear magnetic resonance (NMR) characterizations confirm the successful substitution of Cl for S and the resulting change of P oxidation state from 5+ to 4+, which is also verified by spin moment analysis. Ion transport pathways have been determined with a tracer-exchange NMR method. The functional defects that promote Na ion transport have been maximized for further improvement in ionic conductivity. Full cell performance has been demonstrated using $\text{Na}/\text{Na}_{3.0}\text{PS}_{3.8}\text{Cl}_{0.2}/\text{Na}_3\text{V}_2(\text{PO}_4)_3$ with a reversible capacity of ~ 100 mAh/g at room temperature.

1. Introduction

Sodium (Na)-ion rechargeable batteries, which utilize abundant Na as charge carriers, are an inexpensive alternative to lithium-ion batteries, especially for large-scale energy storage applications.^[1–3]

Solid-state rechargeable batteries, owing to their potential of higher energy density, improved safety, and simplified fabrication process compared with current liquid-based electrolytes, are considered as the next-generation solutions for electrochemical energy storage. Solid electrolytes with fast Na-ion conduction, compatibility with electrodes, processability, and good mechanical properties^[4] are essential to the development of high-performance solid-state rechargeable sodium-ion batteries.

Na solid electrolytes have been commercialized in high-temperature sodium-sulfur batteries using sintered β'' -alumina.^[5] However, the cell operation requires high temperatures above 300 °C which presents several disadvantages in safety, corrosion, and additional power consumption. Na oxide ion conductors such as NASICON electrolytes^[6–8] exhibit high ionic conductivities over 1 mS/cm at room temperature, but their synthesis often necessitates high temperatures of > 1100 °C to reduce grain-boundary resistance. The high sintering temperature and existence of grain boundaries liable for

dendrite formation limit their practical applications. In addition, their chemical, electrochemical, and mechanical compatibility is another challenge to address.

Thiophosphate-based Na-ion conductors with enhanced processability can be incorporated into solid-state batteries with cold press. They can be synthesized at much lower temperatures and often show higher ionic conductivities, compared to Na oxide ionic conductors.

The cubic phase of Na_3PS_4 (c- Na_3PS_4 , an analogue of Li_3PS_4) from the Na_2S - P_2S_5 system was first reported by Hayashi et al. in 2012 with a measured Na^+ conductivity of 0.2 mS/cm.^[9] Further improvement in ionic conductivity has been achieved by Si doping (0.74 mS/cm).^[3,10] Furthermore, substitution of S with larger Se ions increased the ionic conductivity to 1.16 mS/cm and replacement of P with As increased the conductivity to 1.46 mS/cm. though at the expense of reduced electrochemical stability.^[1,11,12] The tetragonal- Na_3PS_4 (t- Na_3PS_4) phase has a low ionic conductivity of 0.05 mS/cm,^[13] which can be significantly improved to reach ~ 1.1 mS/cm by creating structural defects with Cl doping.^[14] In addition, halogen doping promotes the formation of passivating solid-electrolyte interphases, which significantly improves the interfacial stability of thiophosphate-based solid electrolytes when used in all-solid-state batteries.^[14]

In the typical halogen-doped Na_3PS_4 compounds, halide doping for S^{2-} is charge compensated by Na vacancies, i.e., $\text{Na}_{3-x}\text{PS}_{4-x}\text{Cl}_x$, which facilitate Na conductivity. However, the resulting Na deficiency can decrease both the ionic charge carrier concentration and the volume of Na conduction channel, which contributes negatively to the improvement of ionic conductivity. Herein, we report a new synthesis strategy to enhance the ionic conductivity of modified t- Na_3PS_4 . This new strategy is informed by the identification of the functional defects that promote fast ion conduction through un-

Understanding the ion transport mechanism. The synthesis approach is designed to maximize those functional defects and minimize detrimental ones to fast ion conduction.

In the following, we start by presenting the strategic synthesis of fast Na ion conductors with room-temperature ionic conductivities 1.96 mS/cm and activation energy of 0.19 eV ($\text{Na}_{3.0}\text{PS}_{3.8}\text{Cl}_{0.2}$). Then the Na ion conduction mechanism is explained based on the results of tracer-exchange NMR with a discussion of the structure-ion conduction correlation and the rationale for the strategic synthesis. We provide evidence from DFT calculations that independent tuning of Cl doping and Na deficiency helps boosting the Na^+ conductivity. The conversion of P^{5+} to P^{4+} is also observed from both solid-state ^{31}P NMR peak shifting and integrated polarized-spin charge density calculations. The manuscript concludes with a performance demonstration of the new Na solid electrolyte within a full solid-state rechargeable Na-ion battery.

2. Results and discussions

2.1. Synthesis and structural characterizations of $\text{t-Na}_{3-x}\text{PS}_{4-x}\text{Cl}_x$

Two crystal structures of Na_3PS_4 have been reported, tetragonal- and cubic-phase.^[9,13,14] $\text{c-Na}_3\text{PS}_4$ adopts the space group of $I-43m$ with the lattice parameter $a = 6.9965 \text{ \AA}$. while $\text{t-Na}_3\text{PS}_4$ crystallizes in $P-42_1c$ with lattice parameters of $a = 6.9520 \text{ \AA}$ and $c = 7.0757 \text{ \AA}$. These two forms are significantly different in Na positions: in $\text{c-Na}_3\text{PS}_4$, Na is reported to occupy the $12d$ site while in $\text{t-Na}_3\text{PS}_4$, Na sits at both $2a$ and $4d$ sites. Na-ion conductivity is reported to be on the order of 10^{-4} S/cm for glass-ceramic $\text{c-Na}_3\text{PS}_4$,^[9] but this value is much smaller for glass-ceramic $\text{t-Na}_3\text{PS}_4$, 10^{-5} S/cm .^[13,14] The goal of this study is to understand how different structural defects affect Na-ion conduction in usual Cl doped $\text{t-Na}_3\text{PS}_4$ ($\text{Na}_{3-x}\text{PS}_{4-x}\text{Cl}_x$) and to maximize functional defects for enhancing Na-ion conduction.

This article is protected by copyright. All rights reserved.

The insights obtained will be useful for developing other fast-ion conductors. The structure of $t\text{-Na}_3\text{PS}_4$ is shown in **Figure 1a**, in which P is tetrahedrally coordinated with four S. Na_1 and Na_2 occupy $4d$ and $2a$ sites, respectively. Defects in glass-ceramic $t\text{-Na}_3\text{PS}_4$ compounds ($t\text{-Na}_{3-x}\text{PS}_{4-x}\text{Cl}_x$) are created with partial Cl replacement of S in the structure and Na deficiency is generated for charge compensation. The X-ray diffraction (XRD) patterns of $t\text{-Na}_{3-x}\text{PS}_{4-x}\text{Cl}_x$ are shown in **Figure 1b** along with the simulated XRD patterns of $t\text{-}$ and $c\text{-Na}_3\text{PS}_4$. Most of the diffraction peaks in the XRD patterns collected on $t\text{-Na}_{3-x}\text{PS}_{4-x}\text{Cl}_x$ ($x = 0, 0.0625, 0.1, \text{ and } 0.2$) come from $t\text{-Na}_3\text{PS}_4$, except small and broad peaks at around 21° and 44° from the Kapton film and the stainless-steel holder. The XRD patterns of $t\text{-Na}_{3-x}\text{PS}_{4-x}\text{Cl}_x$ ($x = 0, 0.0625, 0.1, \text{ and } 0.2$) only exhibit very slight difference, and the most visible one is the merging of the two diffraction peaks at $2\theta = 30.79^\circ$ and 31.09° . This may suggest the exchange of the two Na sites in $t\text{-Na}_3\text{PS}_4$, which makes the structure gradually converge to $c\text{-Na}_3\text{PS}_4$ with increasing x . In addition, some minor peaks from impurities appear in the sample of $\text{Na}_{2.8}\text{PS}_{3.8}\text{Cl}_{0.2}$, which is consistent with calculation results.^[14] The thermal stability is greatly compromised with increased x value in $t\text{-Na}_{3-x}\text{PS}_{4-x}\text{Cl}_x$.

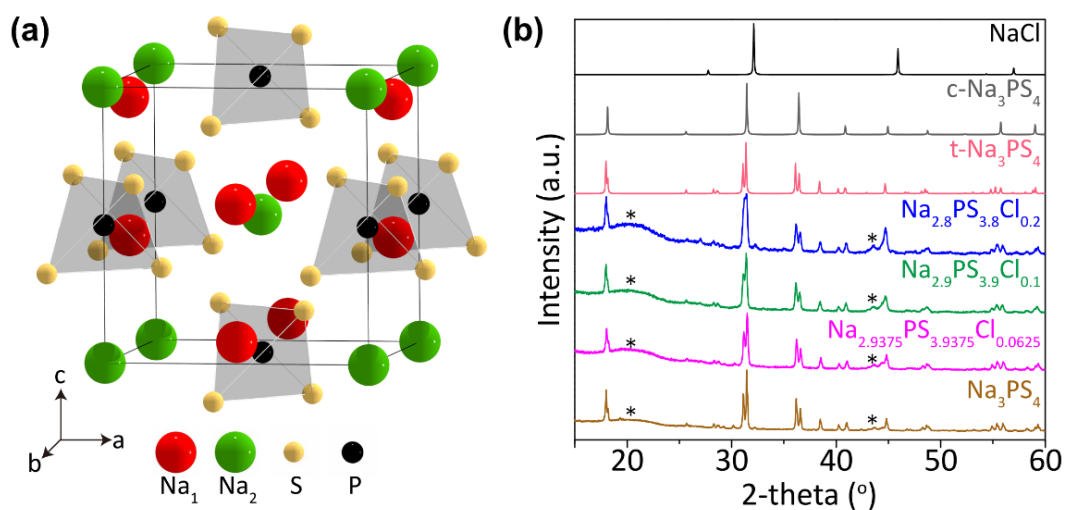


Figure 1. Structure and powder X-ray diffraction characterizations of t-Na_{3-x}PS_{4-x}Cl_x. (a) Crystal structure of pristine tetragonal-Na₃PS₄ (space group = *P*-42₁*c*). Two crystallographically distinct sites Na₁ (4d) and Na₂ (2a), are shown in green and red, respectively. (b) Powder X-ray diffraction patterns of t-Na_{3-x}PS_{4-x}Cl_x (*x* = 0, 0.0625, 0.1, and 0.2). Asterisk (*) indicates the background signals from sample holder and Kapton film.

2.2. Na⁺ conduction in t-Na_{3-x}PS_{4-x}Cl_x

The ionic conductivity of t-Na_{3-x}PS_{4-x}Cl_x (*x* = 0, 0.0625, 0.1, and 0.2) samples is determined with electrochemical impedance spectroscopy (EIS) and the results are shown in **Figure 2a**. The ionic conductivity of t-Na₃PS₄ is $\sim 10^{-5}$ S/cm at room temperature (**Figure 2**), compared with $\sim 10^{-4}$ S/cm for c-Na₃PS₄.^[9] Cl replacement of S in t-Na_{3-x}PS_{4-x}Cl_x leads to significantly improved Na-ion conduction. The highest conductivity of 0.3 mS/cm at room temperature is obtained when *x* equals to 0.1, i.e., t-Na_{2.9}PS_{3.9}Cl_{0.1}. Larger or smaller *x* values yield larger impedance and thus slower ion conduction (**Figure 2a**).

The ionic conductivities of t-Na_{3-x}PS_{4-x}Cl_x are also measured at variable temperatures within the range of 21–120 °C (**Figure S2**) and the results are shown in **Figure 2b**. The activation energy, *E_a*, is determined based on the Arrhenius equation:

This article is protected by copyright. All rights reserved.

$$\sigma = A \cdot \exp\left(\frac{-E_a}{RT}\right) \quad (1)$$

where A is a constant, R is the universal gas constant with the value of $8.314 \times 10^{-3} \text{ kJmol}^{-1}\text{K}^{-1}$, and T is temperature in Kelvin. The activation energy of t-Na₃PS₄ is determined to be 0.34 eV, and it decreases with more Cl → S replacement (0.24 eV for Na_{2.9375}PS_{3.9375}Cl_{0.0625}, 0.23 eV for Na_{2.9}PS_{3.9}Cl_{0.1}, and 0.19 eV for Na_{2.8}PS_{3.8}Cl_{0.2}). As a reference, the activation energy for most solid electrolytes is > 0.24 eV.^[2,14,15] The achieved small activation energy in t-Na_{3-x}PS_{4-x}Cl_x is beneficial for flexible adaptation of these solid electrolytes to be used in different climates especially at low temperatures with no significant decrease in ionic conductivity.

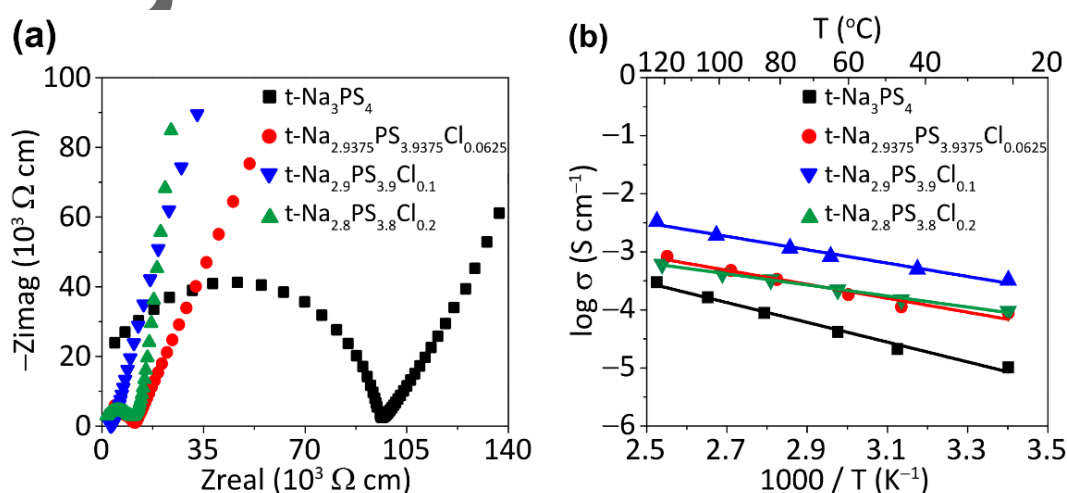


Figure 2. Electrochemical Impedance measurements at 21 °C and Nyquist plots of t-Na_{3-x}PS_{4-x}Cl_x. (a) Nyquist plots of t-Na_{3-x}PS_{4-x}Cl_x (x = 0, 0.0625, 0.1, and 0.2). (b) Arrhenius plot of t-Na_{3-x}PS_{4-x}Cl_x (x = 0, 0.0625, 0.1, and 0.2).

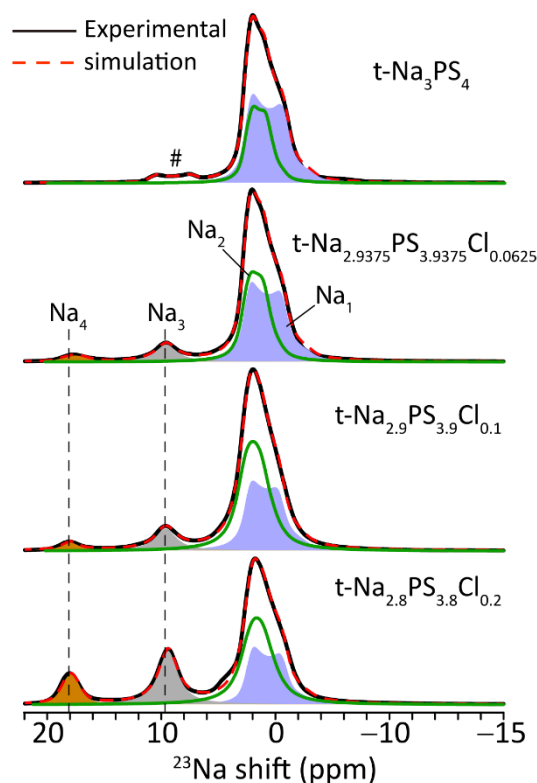
2.3. Solid-state ^{23}Na NMR characterizations of structural defects

Figure 3. Evolution of structural defects in $t\text{-Na}_{3-x}\text{PS}_{4-x}\text{Cl}_x$ ($x = 0, 0.0625, 0.1,$ and 0.2) electrolytes probed by ^{23}Na solid-state magic-angle-spinning (MAS) NMR. ^{23}Na MAS NMR spectra together with simulation results of $t\text{-Na}_{3-x}\text{PS}_{4-x}\text{Cl}_x$ ($x = 0, 0.0625, 0.1,$ and 0.2).

To identify structural features that contribute to Na-ion conduction in $t\text{-Na}_{3-x}\text{PS}_{4-x}\text{Cl}_x$ ($x = 0, 0.0625, 0.1,$ and 0.2), high-resolution solid-state magic-angle-spinning (MAS) ^{23}Na NMR in a high magnetic field of 19.6 T is employed for identifying the local structural environments of Na ions and then tracer-exchange NMR is used to probe Na-ion transport pathways. As shown in **Figure 3**, a clear evolution of ^{23}Na resonances is observed as x increases in $t\text{-Na}_{3-x}\text{PS}_{4-x}\text{Cl}_x$. The ^{23}Na spectrum of $t\text{-Na}_3\text{PS}_4$ shows two main resonance peaks at 3.1 ppm and 3.4 ppm, and the corresponding quadrupolar coupling constants C_Q are 1.7 MHz and 2.3 MHz (See the supporting information). These are assigned to Na_1 and Na_2 sites in the $t\text{-Na}_3\text{PS}_4$ structure. Large C_Q values for Na_1 and Na_2 resonances suggest an

asymmetric structural environment with low Na mobility. In addition to Na₁ and Na₂ resonances, another NMR component appears at 12 ppm with a C_Q value of 2.4 MHz (marked with #). This accounts for 4.5% of the total ²³Na integral and may come from defective sites. Upon partial replacement of S by Cl in t-Na_{3-x}PS_{4-x}Cl_x, two new resonances labeled as Na₃ and Na₄ emerge at 9.6 ppm and 18 ppm with vanished quadrupolar coupling interactions, C_Q = 0. These two ²³Na resonances arise from defective structural sites introduced by the Cl → S replacement, and the amount of these defects increases with the x values in t-Na_{3-x}PS_{4-x}Cl_x (**Figure 3**). In principle, the C_Q values should increase for non-symmetric defective sites. The obtained small C_Qs for Na₃ and Na₄ suggest fast Na-ion motion, which significantly reduces quadrupolar coupling interactions of ²³Na spins. Another evidence of fast Na-ion motion is the significantly larger T₁ relaxation times for Na₃ sites (~ 10 s) compared with those for Na₁ and Na₂ sites (< ~ 0.2 s) in t-Na₃PS₄ (see the supporting information). For Na₁ and Na₂, the ²³Na NMR T₁ relaxation is driven by quadrupolar interactions and the relaxation time is typically on the order of milliseconds, while for Na₃ and Na₄, with the quadrupolar interactions minimized by fast Na motion, the NMR relaxation is driven by other interactions such as dipolar couplings and the typical T₁ relaxation time is on the order of seconds. Na₃ is assigned to Na sites close to Cl and Na₄ to Na sites in the vicinity of Na vacancies, based on the fact that Na₄ resonance is reduced as the Na vacancies are filled, as is discussed later in this work.

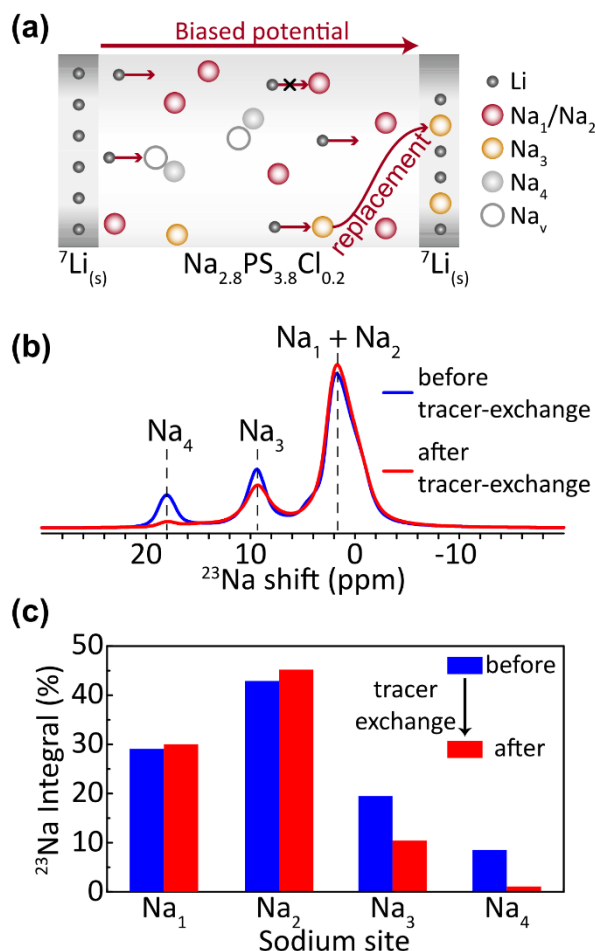
2.4. Na-ion transport mechanism in $t\text{-Na}_{2.8}\text{PS}_{3.8}\text{Cl}_{0.2}$ 

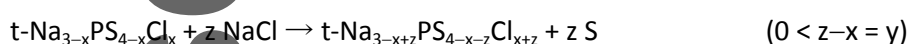
Figure 4. Identification of functional defects with tracer-exchange NMR and ${}^{23}\text{Na}$ solid-state magic-angle-spinning (MAS) NMR. (a) Schematic of electrochemically driven ${}^7\text{Li} \rightarrow {}^{23}\text{Na}$ tracer-exchange method. ${}^{23}\text{Na}$ MAS NMR spectra (b) and quantification (c) of $t\text{-Na}_{2.8}\text{PS}_{3.8}\text{Cl}_{0.2}$ before/after ${}^7\text{Li} \rightarrow {}^{23}\text{Na}$ tracer-exchange.

To understand how the structural defects generated by $\text{Cl} \rightarrow \text{S}$ replacement contributes to the significantly improved ionic conductivity in $t\text{-Na}_{3-x}\text{PS}_{4-x}\text{Cl}_x$, tracer-exchange NMR^[16] is employed to probe Na-ion transport pathways in $t\text{-Na}_{3-x}\text{PS}_{4-x}\text{Cl}_x$. Ideally, these experiments should be carried out by

monitoring the replacement of one Na isotope with another under relevant electrochemical condition. However, as Na has only one isotope, i.e., ^{23}Na , an alternative strategy is adopted by using Li to replace Na driven by a biased electric potential. In the experimental setup, the $t\text{-Na}_{3-x}\text{PS}_{4-x}\text{Cl}_x$ solid electrolyte pellet is sandwiched by two pieces of ^7Li metal (**Figure 4a**). Driven by a biased potential, Li ions diffuse through the solid electrolyte and on the pathway, Li ions replace active Na ions. By identifying at which structural sites Na ions are replaced, the ion transport pathways can be identified. This tracer-exchange experiment is performed on $t\text{-Na}_{2.8}\text{PS}_{3.8}\text{Cl}_{0.2}$ and the results are shown in **Figure 4b** and **4c**. Significant decrease in the intensity of the Na_3 and Na_4 resonances after tracer-exchange and increase in Na_1 and Na_2 resonances are observed. The decrease in Na_4 resonance intensity and increase in Na_1 and Na_2 amount are correlated. Li fills Na vacancies in $t\text{-Na}_{2.8}\text{PS}_{3.8}\text{Cl}_{0.2}$, which leads to the conversion of Na sites next to Na vacancies, i.e., Na_4 , to Na_1 and Na_2 . The decrease in Na_3 amount is due to the replacement of ^{23}Na by ^7Li . The results suggest that Na_3 , which is Na next to Cl, is the active site for ion conduction. This is also confirmed by the positive correlation of enhanced ionic conductivity and the amount of Na_3 in $t\text{-Na}_{2.8}\text{PS}_{3.8}\text{Cl}_{0.2}$. On the other hand, the amount of Na vacancy concentration seems to correlate negatively with the increase in ionic conductivity at higher concentration.

Tracer-exchange NMR provides chemical-specific information on ion transport pathways, identifying the new Na_3 sites as the key for significantly enhanced ion conduction. The 3D diffusion pathways can be visualized from Na^+ probability density distribution (see **Figure S7**). In $t\text{-Na}_{2.9375}\text{PS}_{3.875}\text{Cl}_{0.125}$, 3D diffusion pathways comprise chains of Na_1 sites along the c direction and highly cooperative $\text{Na}_1\text{-Na}_2\text{-Na}_1$ (including those sites converted to Na_3) hopping within ab plane, which form the cubic sub-lattice, similar to that observed in previous studies of Cl-doped Na_3PS_4 .¹⁴

Based on the understanding of ion transport mechanism in $t\text{-Na}_{2.8}\text{PS}_{3.8}\text{Cl}_{0.2}$, to further enhance the ionic conductivity, the amount of Na_3 needs to be increased while Na vacancies should be minimized, which means large x and small y in $t\text{-Na}_{3-y}\text{PS}_{4-x}\text{Cl}_x$. New synthesis strategies are needed to maximize the $\text{Cl} \rightarrow \text{S}$ replacement while preventing significant Na vacancy formation. Following this guideline, we have designed the following reaction to synthesize $t\text{-Na}_{3-y}\text{PS}_{4-x}\text{Cl}_x$ with improved ionic conductivity.



Vacuum is applied to remove the product S during the synthesis, which drives the reaction to proceed to the right. With this method, several compounds are synthesized starting with $t\text{-Na}_{2.9}\text{PS}_{3.9}\text{Cl}_{0.1}$ and $t\text{-Na}_{2.8}\text{PS}_{3.8}\text{Cl}_{0.2}$. The results for $t\text{-Na}_{2.9}\text{PS}_{3.9}\text{Cl}_{0.1}/z\text{NaCl}$ series are presented in the following with the corresponding data for the $t\text{-Na}_{2.8}\text{PS}_{3.8}\text{Cl}_{0.2}/z\text{NaCl}$ series shown in the supporting Information (Figure S8 and Figure S9).

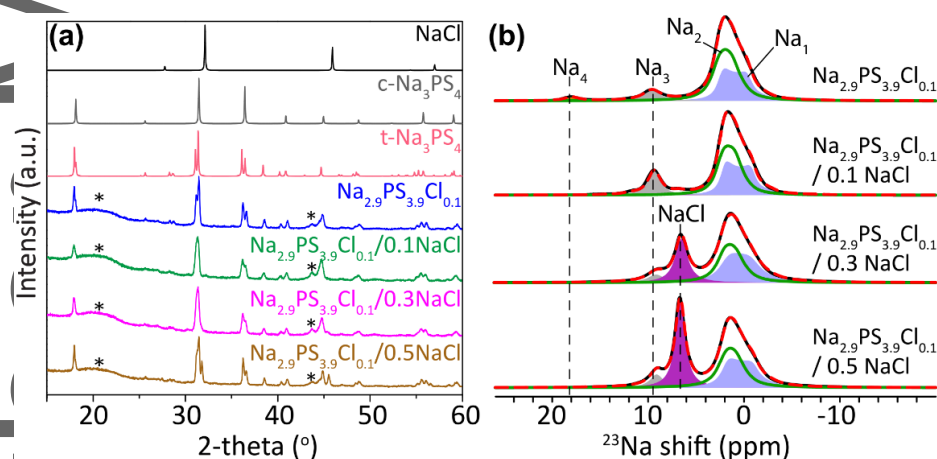


Figure 5. Structure characterizations of synthesized $t\text{-Na}_{2.9}\text{PS}_{3.9}\text{Cl}_{0.1}/z\text{NaCl}$ ($z = 0, 0.1, 0.3, \text{ and } 0.5$). (a) Powder X-ray diffraction patterns (a) and ^{23}Na MAS NMR spectra (b) of $t\text{-Na}_{2.9}\text{PS}_{3.9}\text{Cl}_{0.1}/z\text{NaCl}$ ($z = 0, 0.1, 0.3, \text{ and } 0.5$). Asterisk (*) indicates the background signals from sample holder and polyimide film.

The XRD patterns of the $t\text{-Na}_{2.9}\text{PS}_{3.9}\text{Cl}_{0.1}/z\text{NaCl}$ ($z = 0.1, 0.3, \text{ and } 0.5$) series are shown in **Figure 5a** along with the reference patterns of $t\text{-Na}_3\text{PS}_4$ and NaCl. The incorporation of 0.1 NaCl to $t\text{-Na}_{2.9}\text{PS}_{3.9}\text{Cl}_{0.1}$ is successful, manifested as no observed NaCl diffraction peaks. Also, the additional NaCl modifies the $t\text{-Na}_{2.9}\text{PS}_{3.9}\text{Cl}_{0.1}$ structure to converge to the cubic structure, suggested by the merging of the diffraction peaks at $2\theta = 30.79^\circ$ and 31.09° . When 0.3 NaCl is added to $t\text{-Na}_{2.9}\text{PS}_{3.9}\text{Cl}_{0.1}$, minor NaCl residues are seen from the XRD pattern and the NaCl peaks become obvious with 0.5 NaCl added. To further probe the structural changes induced by the added NaCl, high-resolution ^{23}Na NMR spectra are acquired and presented in Figure 5b. As expected, the addition of 0.1 NaCl to $t\text{-Na}_{2.9}\text{PS}_{3.9}\text{Cl}_{0.1}$ fills the Na vacancies, thus the disappearance of the 18-ppm resonance (Na_4). When more NaCl is added, the resonance from NaCl at 6.6 ppm arises and increases. Summarizing the results from both PXRD and NMR, the z value in $t\text{-Na}_{2.9}\text{PS}_{3.9}\text{Cl}_{0.1}/z\text{NaCl}$ should be less than 0.1 to achieve the goal of partially filling Na vacancies without introducing NaCl impurity. The real formula of $t\text{-Na}_{2.9}\text{PS}_{3.9}\text{Cl}_{0.1}/0.1\text{NaCl}$ should be $t\text{-Na}_{3.0}\text{PS}_{3.8}\text{Cl}_{0.2}$, based on the XRD and NMR results. The optimal z value in $t\text{-Na}_{2.8}\text{PS}_{3.8}\text{Cl}_{0.2}/z\text{NaCl}$ is determined to be 0.2 (**Figure S7**) and the formula for the best sample should be $t\text{-Na}_{3.0}\text{PS}_{3.6}\text{Cl}_{0.4}$.

2.5. Enhanced Na-ion conduction with maximizing functional defects in $t\text{-Na}_{3-y}\text{PS}_{4-x}\text{Cl}_x$

As suggested by tracer-exchange NMR, Na_3 site is responsible for Na conduction. Therefore, Na ionic conductivity can be increased by maximizing $\text{Cl} \rightarrow \text{S}$ replacement and minimizing Na vacancy formation (Na_4). **Figure 6** presents the results of AC impedance measurements on several $t\text{-Na}_{2.9}\text{PS}_{3.9}\text{Cl}_{0.1}/z\text{NaCl}$ ($z = 0.1, 0.3, \text{ and } 0.5$) compounds to validate the proposed strategy. By filling Na

vacancies in $t\text{-Na}_{2.9}\text{PS}_{3.9}\text{Cl}_{0.1}/z\text{NaCl}$ ($z = 0.1, 0.3, \text{ and } 0.5$), the ionic conductivity is increased. The highest ionic conductivity (1.77 mS/cm at 21°C and 1.96 mS/cm at 25 °C) is obtained for $t\text{-Na}_{2.9}\text{PS}_{3.9}\text{Cl}_{0.1}/0.1\text{NaCl}$, nominally $t\text{-Na}_{3.0}\text{PS}_{3.8}\text{Cl}_{0.2}$. For $z = 0.3$ and 0.5, an impurity of NaCl is produced and the observed ionic conductivity is slightly lowered. The activation energy for Na-ion conduction in $t\text{-Na}_{3.0}\text{PS}_{3.8}\text{Cl}_{0.2}$ is determined to be 0.19 eV with variable temperature EIS (**Figure 6b**).

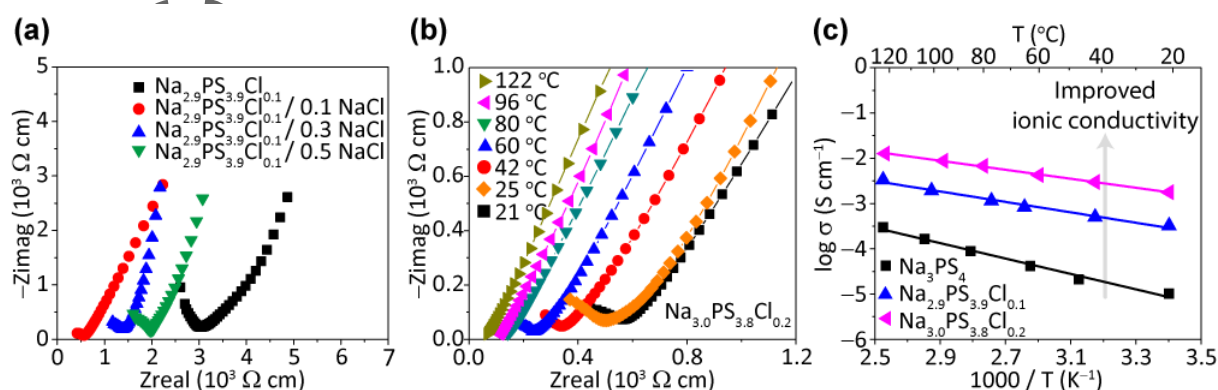


Figure 6. Enhanced ionic conductivities of $t\text{-Na}_{3-x}\text{PS}_{4+x}\text{Cl}_x$. (a) Nyquist plots of $t\text{-Na}_{2.9}\text{PS}_{3.9}\text{Cl}_{0.1}/z\text{NaCl}$ ($y = 0, 0.1, 0.3, \text{ and } 0.5$). (b) Variable-temperature impedance spectra of $t\text{-Na}_{2.9}\text{PS}_{3.9}\text{Cl}_{0.1}/0.1\text{NaCl}$. (c) Arrhenius plots of $t\text{-Na}_3\text{PS}_4$, $t\text{-Na}_{2.9}\text{PS}_{3.9}\text{Cl}_{0.1}$, and $t\text{-Na}_{2.9}\text{PS}_{3.9}\text{Cl}_{0.1}/0.1\text{NaCl}$.

AIMD simulations are performed to verify the doping effect of Cl and Na vacancy in $t\text{-Na}_{3-y}\text{PS}_{4-x}\text{Cl}_x$ ($x = 0.0625$ and 0.125 ; $y = 0, 0.0625, \text{ and } 0.125$) on Na ionic conductivity. The calculated Arrhenius plots for structures with various Cl doping/Na vacancy ratio are shown in **Figure 7**. The conductivity of pristine $t\text{-Na}_3\text{PS}_4$ is poor (< 0.01 mS/cm) but can be increased to 1.38 mS/cm by introducing 2.1% Na vacancy, as reported in previous work.^[14] When Cl concentration increases, we find that the conductivity of $t\text{-Na}_{2.875}\text{PS}_{3.875}\text{Cl}_{0.125}$ can be pushed to a higher value of 6.38 mS/cm, with low activation energy of 0.199 eV. When Na vacancies are partially filled while maintaining the Cl concentration ($\text{Na}_{2.9375}\text{PS}_{3.875}\text{Cl}_{0.125}$), the conductivity is further increased to 9.03 mS/cm and the activation energy is

reduced to 0.174 eV, which is consistent with the experimental results. However, the conductivity decreases sharply to close to that of pristine t- Na_3PS_4 when all Na vacancies are filled ($\text{Na}_3\text{PS}_{4-x}\text{Cl}_x$, $x = 0.0625$ and 0.125). It should be noted that ^{23}Na NMR studies show no sign of Na vacancies for the $\text{Na}_{3.0}\text{PS}_{3.8}\text{Cl}_{0.2}$ nor $\text{Na}_{3.0}\text{PS}_{3.6}\text{Cl}_{0.4}$ which exhibit highest ionic conductivities of all the t- $\text{Na}_{3-y}\text{PS}_{4-x}\text{Cl}_x$ compounds synthesized in this work. This discrepancy is likely due to amount of Na vacancies is too small to be detected. As shown in **Figure 3**, in $\text{Na}_{2.9375}\text{PS}_{3.9375}\text{Cl}_{0.0625}$, Na_4 resonance which represents Na vacancies can be clearly observed. The estimated detection limit of Na vacancies should be much smaller than $0.0625/3 \approx 2\%$.

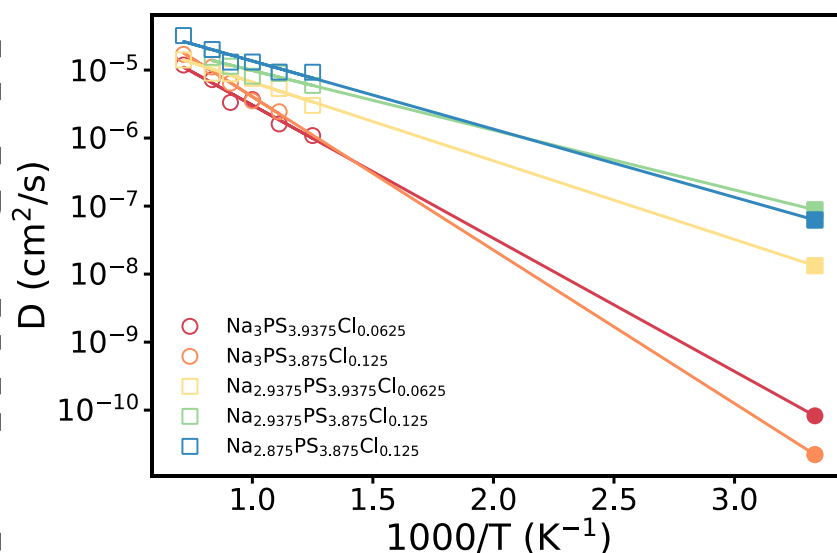


Figure 7. Ionic conductivity of t- $\text{Na}_{3-y}\text{PS}_{4-x}\text{Cl}_x$ from AIMD simulations. Arrhenius plots for $\text{Na}_3\text{PS}_{3.9375}\text{Cl}_{0.0625}$ (red), $\text{Na}_3\text{PS}_{3.875}\text{Cl}_{0.125}$ (orange); $\text{Na}_{2.9375}\text{PS}_{3.9375}\text{Cl}_{0.0625}$ (yellow); $\text{Na}_{2.9375}\text{PS}_{3.875}\text{Cl}_{0.125}$ (green), and $\text{Na}_{2.875}\text{PS}_{3.875}\text{Cl}_{0.125}$ (blue) obtained from AIMD simulations. Squares and circles denote compositions with and without Na vacancies, respectively. Filled circles or squares indicate the extrapolated diffusivities at 300 K.

Topological analyses using open source software^[17] Zeo++ were conducted to assess the free channel volumes for structures with different Cl dopant/Na vacancy ratio. As shown in **Table S5**, when

the Na vacancy was fixed, e.g. $\text{Na}_{2.9375}\text{PS}_{3.9375}\text{Cl}_{0.0625}$ vs. $\text{Na}_{2.9375}\text{PS}_{3.875}\text{Cl}_{0.125}$, the introduction of Cl dopants leads to larger Na channel volumes. In contrast, Na vacancies leads to a decrease in channel volumes. For example, a 2.1% Na vacancy concentration decreases the channel volume from 937 \AA^3 to 924 \AA^3 . From a series of AIMD results, we find that in the presence of small amount of Na vacancy, increase of Cl doping concentration significantly improves the Na^+ conductivity. The calculated channel volume and conductivity results indicates that independent tuning of Cl and Na vacancy amount can lead to optimized conduction performance. Without compensating Na vacancies, the introduction of the Cl^- dopant is charge compensated by the reduction of P, as shown in the next section.

2.6. Change of P oxidation state in $t\text{-Na}_{3-y}\text{PS}_{4-x}\text{Cl}_x$

$\text{Cl} \rightarrow \text{S}$ replacement also leads to changes in the local structural environment of P as seen in ^{31}P NMR (Figure S4). In addition to ^{31}P resonances from $t\text{-Na}_3\text{PS}_4$ at ~ 87 ppm, additional ^{31}P NMR peaks appear between 105–115 ppm for $t\text{-Na}_{3-y}\text{PS}_{4-x}\text{Cl}_x$. P with an oxidation state of 4+ often resonate at a position > 100 ppm, for instance P in $\text{Li}_4\text{P}_2\text{S}_6$ (Li_2PS_3) shows multiple ^{31}P NMR peaks > 105 ppm.^[18] Therefore, these additional ^{31}P resonances observed for $t\text{-Na}_{3-y}\text{PS}_{4-x}\text{Cl}_x$ compounds suggest the conversion of P^{5+} to P^{4+} due to $\text{Cl} \rightarrow \text{S}$ replacement, and the amount of P^{4+} increases with x in $t\text{-Na}_{3-y}\text{PS}_{4-x}\text{Cl}_x$ (Figure S5). Multiple ^{31}P NMR resonances at > 105 ppm suggest an inhomogeneous structural environment due to $\text{Cl} \rightarrow \text{S}$ replacement. Both ^{23}Na and ^{31}P NMR indicate that $\text{Cl} \rightarrow \text{S}$ replacement in $t\text{-Na}_{3-y}\text{PS}_{4-x}\text{Cl}_x$ does not necessarily lead to Na vacancies, instead the charge imbalance due to the replacement can at least be partially compensated by reduction of P^{5+} to P^{4+} . Another evidence for the formation of P^{4+} is the formation of elemental S. We collected the powder evaporated during the synthesis of $\text{Na}_{2.8}\text{PS}_{3.8}\text{Cl}_{0.2}$, and characterized it using XRD. The XRD pattern of the

evaporated powder highly resembles that of the standard S_8 (**Figure S6**). These experimental observations are supported by plotting the spherically integrated spin-polarized charge density of all P ions as a function of cutoff radius from our DFT calculations of $Na_3PS_{3.9375}Cl_{0.0625}$ (**Figure S7**). A non-zero integrated spin was observed ($\sim 1/2\mu_B$ at the radius of 2 Å) for the P in the center of PS_3Cl tetrahedra, indicating the reduction of P^{5+} to P^{4+} . In contrast, all remaining P in PS_4 tetrahedra has negligible net spins, i.e., P^{5+} . Besides, previous reports have suggested based on empirical evidence^[19] that P^{4+} helps to improve the stability of thiophosphate solid electrolytes.

With the formation of P^{4+} , a concern arises that P^{4+} can potentially serve as an electron donor, leading to enhanced electron conduction, while electron conduction is not desirable for solid electrolytes. We have measured the electronic conductivity of both t- Na_3PS_4 and t- $Na_3PS_{3.8}Cl_{0.2}$, and the electronic conductivity of t- $Na_3PS_{3.8}Cl_{0.2}$ is 1.2×10^{-8} S/cm, which is only slightly higher than that for t- Na_3PS_4 , i.e. 0.8×10^{-8} S/cm (Fig. S12). Both values are much lower than the measured ionic conductivity $\sim 2 \times 10^{-3}$ S/cm for t- $Na_3PS_{3.8}Cl_{0.2}$.

2.8. Full cell performance

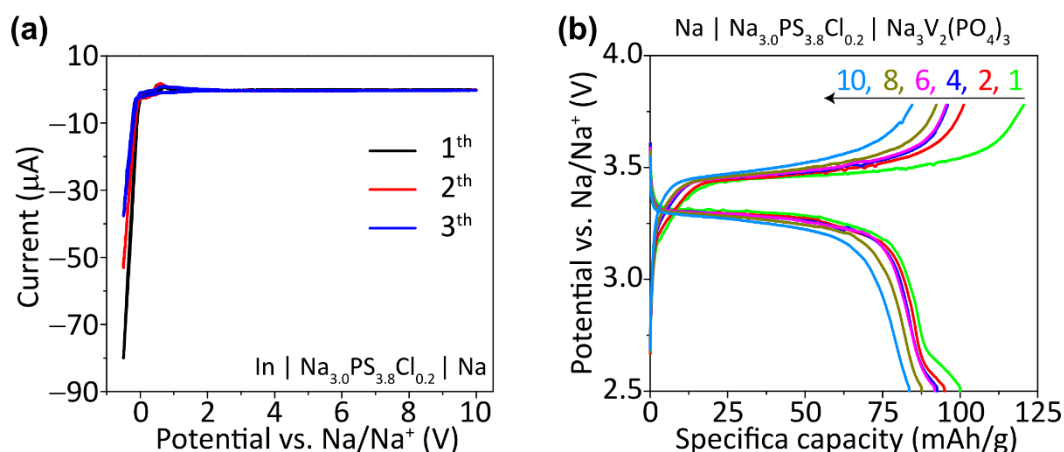


Figure 8. Cyclic Voltammetry and electrochemical performance of a full cell solid-state battery made of $\text{Na} \mid \text{t-Na}_{3.0}\text{PS}_{3.8}\text{Cl}_{0.2} \mid \text{Na}_3\text{V}_2(\text{PO}_4)_3$. (a) CV of a $\text{Na} \mid \text{t-Na}_{3.0}\text{PS}_{3.8}\text{Cl}_{0.2} \mid \text{In}$ cell, (b) The charge and discharge profiles of $\text{Na} \mid \text{t-Na}_{3.0}\text{PS}_{3.8}\text{Cl}_{0.2} \mid \text{Na}_3\text{V}_2(\text{PO}_4)_3$ performed at room temperature with a current density of 10 mA/g calculated based on the mass of $\text{Na}_3\text{V}_2(\text{PO}_4)_3$.

The stability of $\text{t-Na}_{3-y}\text{PS}_{4-x}\text{Cl}_x$ is tested using cyclic voltammetry within a $\text{Na} \mid \text{Na}_{3.0}\text{PS}_{3.8}\text{Cl}_{0.2} \mid \text{In}$ cell. The scan rate is 0.2 mV/s and the battery are cycled between -0.5 V and 10 V (vs. Na/Na^+). As seen in **Figure 8a**, only Na deposition and dissolution occur at around 0 V . No decomposition of $\text{Na}_{3.0}\text{PS}_{3.8}\text{Cl}_{0.2}$ is seen even at a high potential of 10 V , which is attributed to the low electronic conductivity of $\text{Na}_{3.0}\text{PS}_{3.8}\text{Cl}_{0.2}$, limiting the rate of side reactions. The all solid-state Na-ion battery using Na as anode, $\text{Na}_{3.0}\text{PS}_{3.8}\text{Cl}_{0.2}$ as electrolyte, and $\text{Na}_3\text{V}_2(\text{PO}_4)_3$ as cathode achieves a capacity of 100 mAh/g at room temperature (**Figure 8b**) in an initial test, with slight decay over further cycling being observed. The main cause to the capacity decay is interfacial stability upon electrochemical cycling. The impedance of the $\text{Na} \mid \text{Na}_{3.0}\text{PS}_{3.8}\text{Cl}_{0.2} \mid \text{Na}_3\text{V}_2(\text{PO}_4)_3$ full cell before and after cycling is measured and the results are shown in Fig. S13. Before cycling, the total interfacial resistance is only 80 ohms and it increases to $\sim 1300 \text{ ohm}$ after cycling due to non-conductive products formed at electrode-electrolyte interfaces from undesirable side reactions of $\text{Na}_{3.0}\text{PS}_{3.8}\text{Cl}_{0.2}$ with the electrodes (Na anode

and $\text{Na}_3\text{V}_2(\text{PO}_4)_3$ cathode). To improve the electrochemical performance of the full cell using $\text{Na}_{3.0}\text{PS}_{3.8}\text{Cl}_{0.2}$ as the electrolyte, Na-Sn alloy instead of Na should be employed and surface modification of cathode materials is necessary to minimize side reactions of $\text{Na}_{3.0}\text{PS}_{3.8}\text{Cl}_{0.2}$ with the cathode at high potentials.

3. Conclusions

A series of Cl-doped $t\text{-Na}_3\text{PS}_4$ solid electrolytes have been prepared for use in all-solid-state rechargeable Na-ion batteries. Structural analyses have been carried out with techniques including X-ray diffraction and solid-state NMR. In particular, solid-state ^{23}Na MAS NMR identifies the functional defects that promote fast ion conduction. A new synthesis strategy is implemented to maximize the fraction of functional defects while preventing the formation of other defects that impede Na-ion conduction. As a result, the best ionic conductivity is achieved in the composition of $\text{Na}_{3.0}\text{PS}_{2.8}\text{Cl}_{0.2}$, which is about 170 times larger compared with $t\text{-Na}_3\text{PS}_4$, with a low activation energy of 0.19 eV. The P oxidation state changes from 5+ to 4+, which is observed from both NMR and spin moment calculations, allows the introduction of more Cl and less Na vacancy in stable structures of $\text{Na}_{3-y}\text{PS}_{4-x}\text{Cl}_x$. DFT calculations verify that high ionic conductivities can be achieved by independent turning of Na vacancy and Cl-doping. The performance of $\text{Na}_{3.0}\text{PS}_{3.8}\text{Cl}_{0.2}$ is tested in a $\text{Na} \mid \text{Na}_{3.0}\text{PS}_{3.8}\text{Cl}_{0.2} \mid \text{Na}_3\text{V}_2(\text{PO}_4)_3$ cell, which delivers a capacity of 100 mAh/g.

4. Experimental and Computational Section

Synthesis of $t\text{-Na}_{3-y}\text{PS}_{4-x}\text{Cl}_x$ ($0 \leq y \leq x \leq 0.2$) solid electrolytes: $t\text{-Na}_{3-y}\text{PS}_{4-x}\text{Cl}_x$ ($0 \leq y \leq x \leq 0.2$) solid electrolytes were prepared via solid-state reactions. All the chemicals (Na_2S , P_2S_5 , and NaCl) were purchased from Sigma-Aldrich and dried under vacuum at 120 °C overnight before use. Na_2S , P_2S_5 , and

NaCl were weighed inside an Ar-filled glove box and the molar ratios were calculated based on the target compositions. The mixtures were manually ground first, then sealed in a 25-mL ZrO₂ jar under vacuum and ball-milled using a SPEX Sample Prep 8000M mixer for 2 h with two 10-mm ZrO₂ balls as the milling media. The mixtures were then cold-pressed into pellets, which were sintered at 420 °C for 12 h under vacuum with a heating rate of 1 °C/min in a tube furnace (Carbolite MTF). The vacuum environment and temperature gradient generated within the tube furnace facilitate the extraction of S, which favors the replacement of S by Cl. Heating was then turned off to allow the sintered pellets to cool down to room temperature.

Characterizations of t-Na_{3-y}PS_{4-x}Cl_x (0 ≤ y ≤ x ≤ 0.2): The phase identity is examined by powder X-ray diffraction (PXRD). The as-sintered pellets were ground into fine powders and placed in a holder, which was covered by a thin Kapton film to ensure a moisture- and oxygen-free environment. The PXRD patterns were acquired on a Philips X'Pert powder X-ray diffractometer at 45 kV and 40 mA at room temperature by using a Cu-Kα radiation (λ = 1.5406 Å) with a fixed scanning speed of 2°/min from 15° to 60°. The morphologies of t-Na_{3.0}PS_{3.8}Cl_{0.2} were checked by Scanning Electron Microscopy (SEM) on a NOVA NanoSEM 400 field-emission scanning electron microscope.

Solid-state Nuclear Magnetic Resonance (NMR): ²³Na solid-state NMR experiments were performed on a Bruker DRX-830 spectrometer (19.6T) with a home-built 3.2-mm low-E and high-sensitivity magic-angle spinning (MAS) probe. The Larmor frequency of ²³Na is 219.6 MHz. ²³Na spectra were acquired using a single pulse with a solid 90° pulse length of 4.95 μs, a recycle delay of 50 s, and a MAS rate of 16 kHz. ²³Na Spin-lattice relaxation time (T₁) measurements were carried out with a saturation recovery pulse sequence. ²³Na chemical shift was calibrated to a 0.1 M NaCl solution at 0 ppm. ³¹P solid-state NMR spectra were obtained on a Bruker Avance III-500 spectrometer (11.75 T) with a

2.5-mm Bruker HXY MAS probe, operating at a Larmor frequency of 202.4 MHz. ^{31}P spectra were acquired using a rotor-synchronized Hahn-echo pulse sequence with a 90° pulse length of 4.2 μs , a recycle delay of 200 s, and a MAS rate of 25 KHz. ^{31}P chemical shift was calibrated to an 85% H_3PO_4 solution at 0 ppm.

Electrochemical tests: Ionic conductivities of $\text{t-Na}_{3-y}\text{PS}_{4-x}\text{Cl}_x$ pellets at different temperatures were determined using AC impedance measurements. Indium (In) foils with a diameter of 5 mm were attached onto $\text{t-Na}_{3-y}\text{PS}_{4-x}\text{Cl}_x$ pellets as blocking electrodes and current collectors. The sandwiched cell, $\text{In} \mid \text{t-Na}_{3-y}\text{PS}_{4-x}\text{Cl}_x \mid \text{In}$, was then sealed in a home-made cylindrical cell for tests. AC impedance measurements were performed on a Gamry Reference 600⁺ potentiostatic with a perturbation of 50 mV and a scanning frequency from 5 MHz to 1 Hz. Variable-temperature impedance measurements were performed from room temperature to 120 $^\circ\text{C}$. Cyclic voltammetry measurements were carried out on $\text{Na} \mid \text{t-Na}_{3-y}\text{PS}_{4-x}\text{Cl}_x \mid \text{In}$ between -0.5V and 10 V at a scanning rate of 1 mV/s.

Fabrication and performance evaluation of all-solid-state sodium-ion batteries: A full cell was assembled using $\text{Na}_3\text{V}_2(\text{PO}_4)_3/\text{C}$ as cathode, Na metal as anode, and $\text{t-Na}_{3.0}\text{PS}_{3.8}\text{Cl}_{0.2}$ as solid electrolyte. $\text{Na}_3\text{V}_2(\text{PO}_4)_3/\text{C}$ was prepared via a sol-gel process using citric acid as both chelating agent and carbon source. V_2O_5 , $\text{NH}_4\text{H}_2\text{PO}_4$, CH_3COONa , and citric acid (molar ratio 1:3:3.15:2) were dissolved in deionized water first, and then the solution was continuously stirred at 80 $^\circ\text{C}$ to obtain a uniform gel. The gel was then heated at 350 $^\circ\text{C}$ for 5 h and at 800 $^\circ\text{C}$ for another 6 h in an argon atmosphere to obtain the final $\text{Na}_3\text{V}_2(\text{PO}_4)_3/\text{C}$ cathode. The solid electrolyte $\text{t-Na}_{3.0}\text{PS}_{3.8}\text{Cl}_{0.2}$ (50 mg) was cold-pressed using a 6-mm stainless steel die and then 5 mg composite cathode which contains 60% $\text{t-Na}_{3.0}\text{PS}_{3.8}\text{Cl}_{0.2}$ and 40% $\text{Na}_3\text{V}_2(\text{PO}_4)_3/\text{C}$ was pressed on top of the $\text{t-Na}_{3.0}\text{PS}_{3.8}\text{Cl}_{0.2}$ electrolyte layer. Pure Na metal was pressed into a thin film which was attached to the opposite site of the $\text{t-Na}_{3.0}\text{PS}_{3.8}\text{Cl}_{0.2}$ anode. The

This article is protected by copyright. All rights reserved.

whole battery was sealed in a home-made cylindrical cell and cycled at current density of 10 mA/g calculated based on the mass of $\text{Na}_3\text{V}_2(\text{PO}_4)_3$ within a voltage window of 2.5V–3.8V.

Density functional theory (DFT) calculations: All DFT calculations were performed using the Vienna Ab initio Simulation Package (VASP)^[20] within the projector augmented-wave approach.^[21] Similar parameters were used as previous works by the authors.^[14,22,23] Briefly, all calculations were performed using the Perdew-Burke-Ernzerhof (PBE) generalized-gradient approximation (GGA) functional.^[24] For each composition (Na and Cl concentration), we carried out spin-polarized structure relaxation and total energy calculations of all symmetrically distinct configurations of $\text{v}'_{\text{Na}} - \text{Cl}'_{\text{S}}$ in a $2 \times 2 \times 2$ supercell of t- Na_3PS_4 (16 formula units) using parameters consistent with those in Materials Project (MP),^[25] i.e., an energy cutoff of 520 eV and a k-point mesh of at least 1000/atom. The lowest energy configuration was then selected for the subsequent calculations and analyses.

Non-spin-polarized AIMD simulations were performed for t- $\text{Na}_{3-y}\text{PS}_{4-x}\text{Cl}_x$ at $x = 0.0625$ and 0.125 and $y = 0, 0.0625,$ and 0.125 in an NVT ensemble at elevated temperatures with a Nose–Hoover thermostat.^[26,27] A smaller plane-wave energy cutoff of 280 eV, a minimal Γ -centered $1 \times 1 \times 1$ k-point mesh, and a time step of 2 fs were adopted. The simulation supercell sizes were around 14 \AA ($2 \times 2 \times 2$ supercell) along each lattice direction. The structures were fully relaxed at 0 K and the volumes were fixed for AIMD at elevated temperatures (800 K–1400 K). No framework melting observed at the temperatures we adopted. The Na^+ diffusivity was calculated using the Einstein relation $D = \frac{1}{2dt} \langle [\Delta \vec{r}^2(t)] \rangle$, where d is the dimensionality of diffusion ($=3$ for 3D conductors here) and $[\Delta \vec{r}^2(t)]^2$ is the average Na^+ mean square displacement (MSD) over a time duration t . The diffusivity was obtained via a linear fitting of the MSD with time. Arrhenius plots were constructed to determine the

activation energies and obtain extrapolated room-temperature diffusivities D_{300K} . We derived the room-temperature Na ion conductivity from the Nernst-Einstein equation, $\sigma_{300K} = \frac{\rho z^2 F^2}{RT} D_{300K}$ where ρ is the molar density of diffusing Na ions in the unit cell; $z = 1$ is the charge of Na ions; and F and R are the Faraday's constant and the gas constant respectively. $T = 300$ K was used in the above equation.

The Python Materials Genomics (pymatgen)^[28] materials analysis library was used for all analyses and structure generation.

Supporting Information

Supporting Information is available from the Wiley Online Library or from the author.

Acknowledgements

This work is supported by the National Science Foundation under Grant No. DMR-1808517. All the NMR experiments are carried out at the NHMFL, which is funded by the state of Florida and NSF (DMR-1157490). The DFT studies are supported by the U.S. Department of Energy, Office of Science, Basic Energy Sciences under Award No. DESC0012118. We also acknowledge computational resources provided by Triton Shared Computing Cluster (TSCC) at the University of California, San Diego, the National Energy Research Scientific Computing Center (NERSC), and the Extreme Science and Engineering Discovery Environment (XSEDE) supported by National Science Foundation under Grant No. ACI-1053575.

Conflict of Interest

The authors declare no conflict of interests.

Keywords

sodium solid electrolyte, all-solid-state sodium-ion batteries, thiophosphate

Received: ((will be filled in by the editorial staff))

Revised: ((will be filled in by the editorial staff))

Published online: ((will be filled in by the editorial staff))

- [1] Z. Yu, S.-L. Shang, J.-H. Seo, D. Wang, X. Luo, Q. Huang, S. Chen, J. Lu, X. Li, Z.-K. Liu, D. Wang, *Adv. Mater.* **2017**, *29*, 1605561.
- [2] W. D. Richards, T. Tsujimura, L. J. Miara, Y. Wang, J. C. Kim, S. P. Ong, I. Uechi, N. Suzuki, G. Ceder, *Nat. Commun.* **2016**, *7*, 11009.
- [3] N. Tanibata, K. Noi, A. Hayashi, M. Tatsumisago, *RSC Adv* **2014**, *4*, 17120.
- [4] Z. Deng, Z. Wang, I.-H. Chu, J. Luo, S. P. Ong, *J. Electrochem. Soc.* **2016**, *163*, A67.
- [5] K. B. Hueso, M. Armand, T. Rojo, *Energy Environ. Sci.* **2013**, *6*, 734.
- [6] H.-P. Hong, *Mater. Res. Bull.* **1976**, *11*, 173.
- [7] O. Bohnke, S. Ronchetti, D. Mazza, *Solid State Ion.* **1999**, *122*, 127.
- [8] J. B. Goodenough, H.-P. Hong, J. A. Kafalas, *Mater. Res. Bull.* **1976**, *11*, 203.
- [9] A. Hayashi, K. Noi, A. Sakuda, M. Tatsumisago, *Nat. Commun.* **2012**, *3*, 856.
- [10] Z. Zhu, I.-H. Chu, Z. Deng, S. P. Ong, *Chem. Mater.* **2015**, *27*, 8318.
- [11] S.-H. Bo, Y. Wang, G. Ceder, *J Mater Chem A* **2016**, *4*, 9044.
- [12] H. M. Tang, Z. Deng, Z. N. Lin, Z. B. Wang, I.-H. Chu, C. Chen, Z. Y. Zhu, C. Zheng, S. P. Ong, *Chem. Mater.* **2017**, *30*, 163.
- [13] M. Jansen, U. Henseler, *J. Solid State Chem.* **1992**, *99*, 110.
- [14] I.-H. Chu, C. S. Kompella, H. Nguyen, Z. Zhu, S. Hy, Z. Deng, Y. S. Meng, S. P. Ong, *Sci. Rep.* **2016**, *6*.
- [15] M. Duchardt, U. Ruschewitz, S. Adams, S. Dehnen, B. Roling, *Angew. Chem. Int. Ed.* **2018**, *57*, 1351.
- [16] J. Zheng, M. Tang, Y.-Y. Hu, *Angew. Chem. Int. Ed.* **2016**, *55*, 12538.

This article is protected by copyright. All rights reserved.

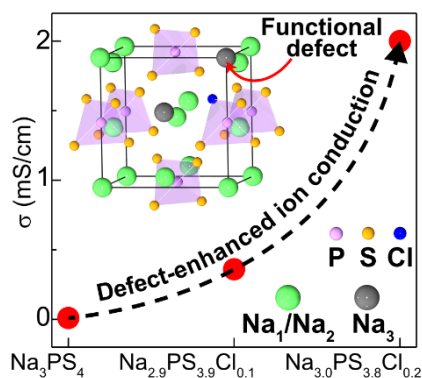
- [17] T. F. Willems, C. H. Rycroft, M. Kazi, J. C. Meza, M. Haranczyk, *Microporous Mesoporous Mater.* **2012**, *149*, 134.
- [18] S. Neuberger, S. P. Culver, H. Eckert, W. G. Zeier, J. Schmedt auf der Günne, *Dalton Trans.* **2018**, *47*, 11691.
- [19] Y. Kato, S. Hori, T. Saito, K. Suzuki, M. Hirayama, A. Mitsui, M. Yonemura, H. Iba, R. Kanno, *Nat. Energy* **2016**, *1*, 16030.
- [20] G. Kresse, J. Furthmüller, *Phys. Rev. B* **1996**, *54*, 11169.
- [21] P. E. Blöchl, *Phys. Rev. B* **1994**, *50*, 17953.
- [22] Z. Deng, Z. Zhu, I.-H. Chu, S. P. Ong, *Chem. Mater.* **2017**, *29*, 281.
- [23] Z. Zhu, I.-H. Chu, S. P. Ong, *Chem. Mater.* **2017**, *29*, 2474.
- [24] J. P. Perdew, K. Burke, M. Ernzerhof, *Phys. Rev. Lett.* **1996**, *77*, 3865.
- [25] A. Jain, S. P. Ong, G. Hautier, W. Chen, W. D. Richards, S. Dacek, S. Cholia, D. Gunter, D. Skinner, G. Ceder, K. A. Persson, *APL Mater.* **2013**, *1*, 011002.
- [26] S. Nosé, *J. Chem. Phys.* **1984**, *81*, 511.
- [27] W. G. Hoover, *Phys. Rev. A* **1985**, *31*, 1695.
- [28] S. P. Ong, W. D. Richards, A. Jain, G. Hautier, M. Kocher, S. Cholia, D. Gunter, V. L. Chevrier, K. A. Persson, G. Ceder, *Comput. Mater. Sci.* **2013**, *68*, 314.

A highly conductive sodium solid electrolyte $\text{Na}_{3-y}\text{PS}_{4-x}\text{Cl}_x$ is obtained as a result of a characterization-informed synthesis. Functional defects for fast Na-ion conduction are first identified via short-range structural characterizations and then strategically created through controlled synthesis. The impact of structural defects in $\text{Na}_{3-y}\text{PS}_{4-x}\text{Cl}_x$ is also investigated with computational studies.

Keyword: sodium solid electrolyte, all-solid-state sodium-ion batteries, thiophosphate

Xuyong Feng, Po-Hsiu Chien, Zhuoying Zhu, Iek-Heng Chu, Pengbo Wang, Marcello Immediato-Scuotto, Hesam Arabzadeh, Shyue Ping Ong, and Yan-Yan Hu*

Studies of Functional Defects for Fast Na-ion Conduction in $\text{Na}_{3-y}\text{PS}_{4-x}\text{Cl}_x$ with a Combined Experimental and Computational Approach



This article is protected by copyright. All rights reserved.